Article

Extended Single-Electron Transfer Model and Dynamically Associated Energy Transfer Event in a Dual-Functional Catalyst System

Xiaorui Zhang, Lin Liu, Weijia Li, Chu Wang, Juanjuan Wang,* Wei-Hai Fang, and Xuebo Chen*

Read Online

ACCESS | 📊 Metrics & More | 📖 Article Recommendations | 🆂🅸 Supporting Information

ABSTRACT: Organic photocatalysis has been developed flourishingly to rely on bimolecular energy transfer (EnT) or oxidative/reductive electron transfer (ET), promoting a variety of synthetic transformations. However, there are rare examples to merge EnT and ET processes rationally within one chemical system, of which the mechanistic investigation still remains in its infancy. Herein, the first mechanistic illustration and kinetic assessments of the dynamically associated EnT and ET paths were conducted for realizing the C−H functionalization in a cascade photochemical transformation of isomerization and cyclization by using the dual-functional organic photocatalyst of riboflavin. An extended single-electron transfer model of transition-state-coupled dual-non-adiabatic crossings was explored to analyze the dynamic behaviors in the proton transfer-coupled cyclization. This can also be used to clarify the dynamic correlation with the EnT-driven $E \rightarrow Z$ photoisomerization that has been kinetically evaluated by using Fermi's golden rule with the Dexter model. The present computational results of electron structures and kinetic data contribute to a fundamental basis for understanding the photocatalytic mechanism of the combined operation of EnT and ET strategies, which will guide the design and manipulation for the implementation of multiple activation modes based on a single photosensitizer.

KEYWORDS: *energy transfer, electron transfer, dynamic correlation, kinetic evaluation, aromatic C−H functionalization*
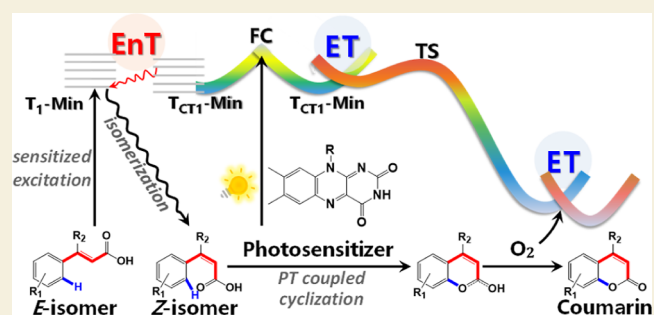
O rganocatalysis has vastly expanded over 20 years and is gradually developing into one of the three pillars besides the counterparts of metal catalysis and biocatalysis in the area of catalysis.[1−3] Dating back to 1859, Liebig showed the first example of organocatalysis, in which the pure organic molecule of acetaldehyde was used to achieve a catalytic organic transformation from cyanogen to oxamide.[2,4] However, the chemical synthesis community overlooked the research field of organocatalysis in the following one-and-a-half centuries.[5−7] This situation was altered significantly until 2000 by the exploration of a new type of reaction of organic enamine[5] and iminium[6] catalysis, leading to the frequent utilization of the conception of "organocatalysis". Moreover, the pioneer works of List and MacMillan demonstrated that small organic molecules could catalyze the same chemical reactions as much larger organic molecules following a similar mechanism.[5−9] The rapid expansion of organocatalysis can be attributed to many advantages of organic small-molecule catalysts in comparison to metal catalysts, including relative nontoxicity, availability from natural biological sources, as well as air and water stability.[7,10] These further promote organocatalysis to serve as an effective platform to meet operational requirements of industrial applications on the merits of the concise experimental procedure, atom economy, and reduction

in time and energy cost.[1,7] However, this synthesis method is merely applicable to a limited amount of reactions since it generally requires prefunctionalization of substrates,[11] introduction of sacrificial agents,[12−14] or suffers from harsh reaction conditions such as high temperature[15,16] and high pressure[17,18] in most cases.

To circumvent these obstacles, in 2007, MacMillan and co-workers developed the third aminocatalysis mode of one-electron activation, in which a more susceptible radical cation was generated with a 3π-electron configuration bearing a more energetically favorable singly occupied molecular orbital compared with the case of the two-electron pathway.[19−23] Inspired by this advance, the MacMillan group further exploited a combined scheme of enamine catalysis with photoredox catalysis to directly use abundant visible-light resources.[24] This allows the occurrence of photocatalysis under

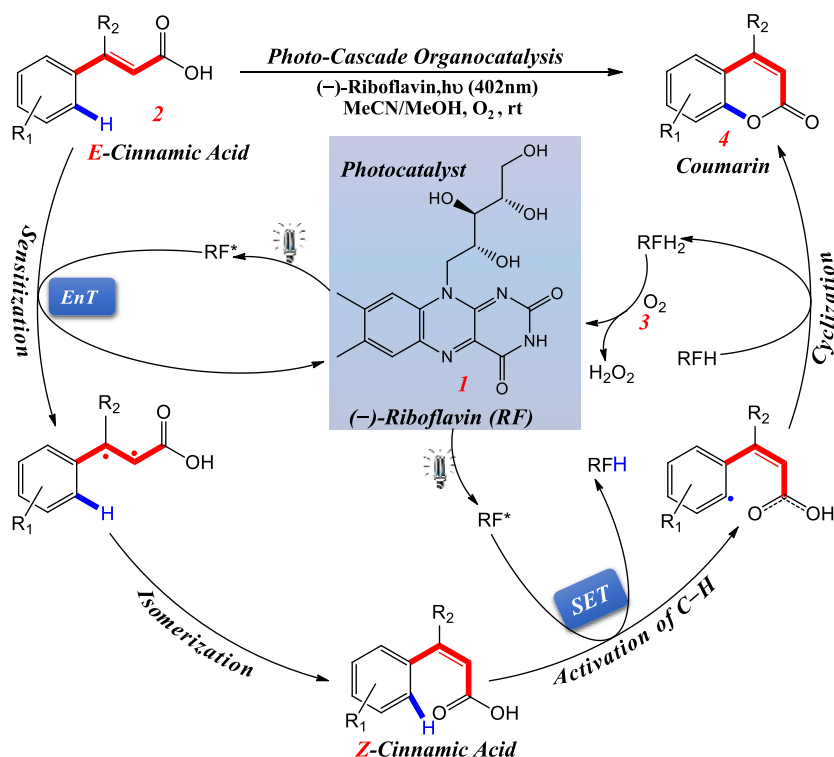**Scheme 1. Schematic Illustration of Cascade Catalysis Reaction to Emulate Coumarin Derivative Biosynthesis Merging EnT and SET Activation Modes Mediated by the (−)-Riboflavin Photocatalyst**

mild conditions to produce the radical intermediate through the single-electron transfer (SET) reaction between the excited-state Ru(bpy)$_3$Cl$_2$ and alkyl bromide.[24] Following a similar philosophy, the organic small molecule of *p*-anisaldehyde was used as a photosensitizer to activate haloalkane substrates, in which the photocatalytic rates are sensitively correlated with the triplet-state energies of photosensitizers, supporting an EnT mechanism.[25] As a coexisting approach, EnT photo-organocatalysis has taken advantage of the vacancy of electron transfer (ET), which overcomes the current limitations of the ET path regarding the incompatible redox potentials of substrates with excited photocatalysts.[26−31] In the past decade, the combined EnT and ET strategies have been applied in a novel photo-organocatalysis to make the unification of two discrete catalytic cycles, thereby allowing multiple activation modes based on one photocatalyst.[28,32] As shown in Scheme 1, Gilmour and his co-workers employed (−)-riboflavin as a photocatalyst to catalytically activate the simple substrate of *E*-cinnamic acids instead of the phenol-derived starting material, thus sequentially inducing EnT-mediated isomerization followed by cyclization along the ET path.[33,34] Consequently, the dynamically correlated processes of EnT and ET proceed smoothly without changing reaction conditions, which requires a well-balanced scheme for dynamically controlling pathways. Most importantly, this newly emerged approach emulates the coumarin biosynthesis pathway to afford the *Z*-isomers, while SET-driven cyclization eliminates the requisite step for preparing a prefunctionalized aryl ring.[34]
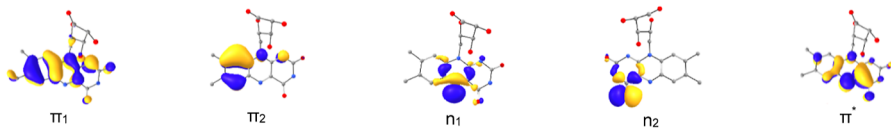
The combined approach also offers other advantages, especially for the efficient activation of aromatic C−H bonds under visible-light irradiation (ca. 400 nm). The aromatic C−H bonds abundantly exist and exhibit higher bond dissociation energies (ca. 110−118 kcal/mol)[35] than C−C or C−X bonds,

which limits their application to suffer from the narrow substrate scope and poor selectivity.[35−37] Since the year 2008, many visible-light organic photocatalysts such as eosin Y,[38] rhodamine 6G,[39] PDI,[40] riboflavin, and riboflavin tetraacetate[41,42] have been continuously inspected to create a powerful platform for implementing aromatic C−H bond functionalization.[26,43,44] In other words, the utilization of visible-light-driven organocatalysis enables easy access to various aromatic C−H functionalizations imposed by the photosensitized EnT and ET along the energetically least costly paths. The question is how to compensate for the energy shortages between the energy consumption of aromatic C−H bond dissociation and the input energies of visible-light irradiation (ca. 400 nm). Therefore, there is an urgent need for efforts in mechanistic exploration to provide the structural and energetic basis for understanding the dynamic routes of excitation-energy relaxation associated with structural evolution. On the other hand, the kinetic and thermodynamic evaluations should be considered to disclose key factors for controlling photosensitized arene C−H bond functionalization, especially for dynamically correlated EnT and ET photocatalysis as shown in Scheme 1.[34]

In our previous works, mechanistic analyses and kinetic assessments were separately applied to a series of photosensitized EnT and ET catalysis reactions mediated by transition or actinide metal complexes.[45−47] Herein, the combined EnT and ET processes will be considered simultaneously for the first time in the cascade catalysis of isomerization and cyclization photosensitized by the organic photocatalyst of (−)-riboflavin (see Scheme 1). In this work, the multiconfiguration perturbation theory at the second-order perturbation (CASPT2) level with a complete active space self-consistent field (CASSCF) reference function was employed to map minimum-energy profiles (MEPs) in excited and ground

Table 1. Vertical Excitation Energies (ΔE_{ve}, eV/nm) Are Summarized to Compare with the Experimental Values in Parentheses If Available,[66,67,71] Together with Oscillator Strengths (f), Dipole Moment Changes (ΔD.M., Debye), as well as the Characters of Singly Occupied Orbitals for Various Electronic Transitions of Photocatalyst 1[a]

Transitions	ΔE_{ve}	f	ΔD.M.	Singly occupied orbitals
$S_0 \rightarrow S_{CT1}(^1\pi\pi^*)$	2.93/423 (439[exp.])	0.35	$10.8 \rightarrow 15.5$	$\pi_1 \rightarrow \pi^*$
$S_0 \rightarrow S_{CT2}(^1\pi\pi^*)$	3.86/321 (350[exp.])	0.13	$10.8 \rightarrow 15.2$	$\pi_2 \rightarrow \pi^*$
$S_0 \rightarrow S_3(^1n\pi^*)$	4.00/310	0.01	$10.8 \rightarrow 10.4$	$n_1 \rightarrow \pi^*$
$S_0 \rightarrow S_4(^1n\pi^*)$	4.31/287	$< 10^{-3}$	$10.8 \rightarrow 7.7$	$n_2 \rightarrow \pi^*$
$S_0 \rightarrow T_{PP1}(^3\pi\pi^*)$	2.81/441	$< 10^{-7}$	$10.8 \rightarrow 10.0$	$\pi_1 \rightarrow \pi^*$

π_1 π_2 n_1 n_2 π^*

[a]The values were computed in the acetonitrile matrix at the CASPT2//RASSCF (14e/12o)/PCM level of theory.

states for the photogenerated *Z*-isomer of cinnamic acids and subsequent SET-based photocyclization via a photosensitization manner. Based on highly accurate calculations of the molecular electronic structure, the physical parameters for rate calculations of EnT, ET, and the subsequent photocyclization reaction can be obtained to perform kinetic assessments and establish the theoretical model associated with the reaction mechanism exploration and regulation strategy of cascade photo-organocatalysis.

■ METHODS

The *ab initio* electronic structure calculations of the photocatalyst (−)-riboflavin (**1**), the substrate of 3-phenylhex-2-enoic acid (**2**), as well as **1-2** and **1-2-3** (O_2) complexes, were primarily performed at the CASSCF level of theory. To perform multiconfigurational CASSCF calculations, numerous test calculations are generally required to obtain an appropriate active space that can be used to represent a variety of electronic states and photochemical reactions, including but not limited to different types of charge-transfer (CT) transitions, the $E \rightarrow Z$ isomerization, EnT and SET processes, and the proton transfer-coupled cyclization. Based on the numerous test calculations, the active space was carefully selected to reasonably reduce the computational burden but without losing important physical and chemical information concerning the electron transition, as well as bond breakage and formation, thereby achieving the balance of computational efficiency and accuracy. In brief, a total of 14e/12o and 10e/9o active space with 5-root state-averaging was employed for the isolated **1** and **2**. A total of 12e/11o and 14e/12o active space with 6-root state-averaging was employed for **1−2** and **1−2−3** complexes, respectively.

All local minima were obtained by CASSCF optimizations, and the intersections were optimized via the minimum-energy crossing point method. The MEPs were mapped by the intrinsic reaction coordinate (IRC) calculations based on the obtained minima and their crossings. To consider dynamic electron correlation effects, the refined single-point energy was recalculated at the CASPT2 level of theory based on the zeroth-order multiple-root state-averaged CASSCF wave functions. The preliminary geometry optimizations and frequency analyses for all stationary points (minima and transition states) were calculated at the density functional theory (DFT) or time-dependent density functional theory level using the B3LYP functional. The results of frequency analyses on minima were employed for EnT rates and transition-state rates. The solvent effect was included using the polarizable continuum model (PCM, acetonitrile) for all computations. The reductive and oxidative SET rate constants of the photocatalyst were calculated using the formula of Marcus ET theory.[48−51] The electronic coupling matrix elements were estimated by the generalized Mulliken−Hush method[52−54] for singlet−singlet

couplings and the spin−orbit-Hamiltonian matrix elements[55,56] for the singlet−triplet interaction. The rate constant of proton transfer-coupled cyclization involving the transition state was estimated by canonical variational transition-state theory.[57−60] The triplet−triplet EnT rates were estimated using Fermi's golden rule combined with the Dexter model that is the generally adopted formalism for rate calculation of nonradiative transition.[61−63] All of the DFT, CASSCF, and IRC computations and the TD-DFT computations were performed using the Gaussian program package,[64] while the CASPT2 calculations were conducted employing the Molcas 8.0 program package.[65] For more computational details, see the Supporting Information.

■ RESULTS AND DISCUSSION

Photochemical Properties and Relaxation Pathway for the Riboflavin-Based Visible-Light Catalyst

To disclose the origin of visible-light absorption and the photocatalytic activity of riboflavin, the excitation energies together with its photochemical properties and the visible-light-driven relaxation path for photocatalyst **1** used in this work were calculated at the CASPT2//CASSCF(14e/12o)/PCM level of theory and are summarized in Table 1 and Figure 1. A pair of bright spectroscopic states, i.e., $S_{CT1}(^1\pi\pi^*)$ and $S_{CT2}(^1\pi\pi^*)$, were found for isolated **1** to exhibit a similar magnitude of the oscillator strengths (f = 0.32 and 0.15). Population analyses demonstrated that low-lying bright states originate from the electron promotions of two energetically
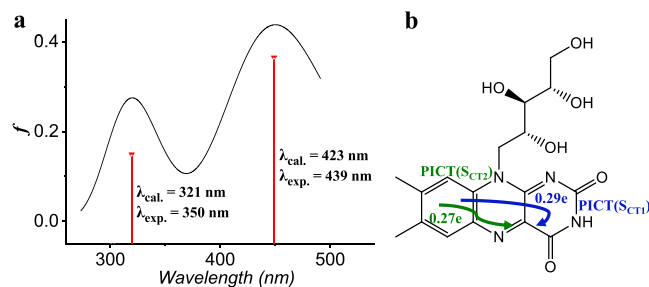

Figure 1. (a) Calculated absorption spectra (cal.) for photosensitizer **1** in the acetonitrile matrix in comparison with experimentally measured values (exp.). (b) Diagrams of PICT are shown to disclose the origin of two bright spectroscopic bands. The results were obtained in the acetonitrile matrix at the CASPT2//RASSCF (14e/12o)/PCM level of theory.

degenerate π orbitals (S_{CT1}: π_1; S_{CT2}: π_2) localized in the dimethyl-phenyl moiety to the pyrazinyl centered π_1^* orbital, exhibiting obvious characteristics of spatial separation (see Table 1). Therefore, the $S_0 \rightarrow S_{CT1}$ and S_{CT2} transitions exhibit the CT characteristics, which can be further evidenced by charge relocation calculation with $0.27e$ (S_{CT1}) and $0.29e$ (S_{CT2}) charge immigration from the dimethyl-phenyl to the pyrazinyl moiety, as shown in Figure 1b. Specific features of the CT states (S_{CT1} and S_{CT2}) stem from the natural donor (D)−acceptor (A) structure generated in bioevolution, which is further enhanced in the presence of the electron-donating dimethyl group in the donor moiety and the electron-withdrawing carbonyl group in pyrimidine. These structural advantages promote photoinduced CT (PICT) in the excitation processes along the desired D−A direction. As an important result, the absorption spectrum of riboflavin is red-shifted to the visible region. The vertical excitation energies for **1** are calculated to be 423 (S_{CT1}) and 321 (S_{CT2}) nm at the CASPT2//CASSCF/PCM (MeCN) level of theory, which well reproduces the experimentally measured values located at 439 and 350 nm in acetonitrile matrix.[66,67] Introduction of a strong electron-donating group (i.e., *N,N*-dimethyl in rose-oflavin) on the phenyl moiety improves the corresponding PICT to exhibit a significant spectral red shift from 423 nm (riboflavin) to 487 nm (roseoflavin).[66] The present computational pieces of evidence reveal that the naturally evolved D−A skeleton (i.e., isoalloxazine moiety) imposes a tunable PICT for the riboflavin-based photocatalyst/photosensitizer to utilize a completely abundant source of visible light. Meanwhile, two optically dark states were also determined and assigned to be n $\rightarrow \pi^*$ transitions originating from electron promotion of lone pairs of N1 (S_3) and O2 (S_4) in the pyrazine ring, respectively.

As shown in Figure 2, upon visible-light photoexcitation, photocatalyst **1** is initially populated in the Franck−Condon
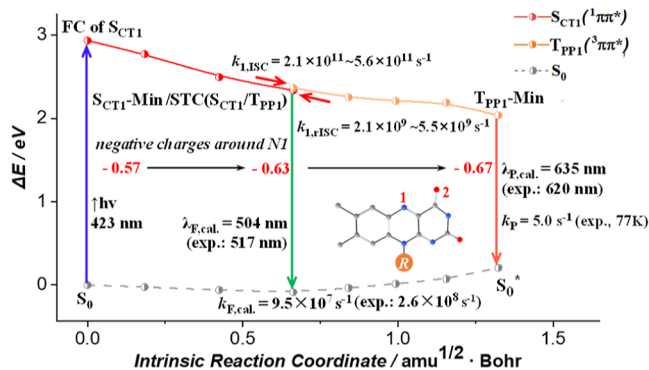

Figure 2. Radiative relaxation pathway of photocatalyst **1** computed in the acetonitrile matrix at the CASPT2//CASSCF/PCM level of theory. The key photophysical parameters are provided along the relaxation path. Negative charge evolution around N1 was obtained by using the Mulliken population analyses.

(FC) region of the $S_{CT1}(^1\pi\pi^*)$ state and rapidly decays to its minimum, S_{CT1}-Min, which is energetically 0.68 eV below the FC point following a downhill relaxation path. Fluorescence emission is theoretically predicted at 504 nm from S_{CT1}-Min, which closely correlates with experimentally measured values (517−543 nm).[66] Moreover, the critical point of S_{CT1}-Min energetically degenerates with its triplet state of $T_{PP1}(^3\pi\pi^*)$ and is therefore denoted as the singlet−triplet crossing (STC) of STC($^1\pi\pi^*$/$^3\pi\pi^*$). The existence of anti-El-Sayed-type

crossing is largely ascribed to an acceptable spin−orbit-coupling (SOC: 5.3−8.6 cm^{-1}) for pure organic photocatalyst **1**, which further promotes the occurrence of intersystem crossing (ISC) with high efficiency ($k_{1,ISC} = 2.1 \times 10^{11}$ to 5.6×10^{11} s^{-1}) between singlet and triplet states with the same original feature of $\pi \rightarrow \pi^*$ transition. Consistently, photocatalyst **1** was experimentally measured to exhibit a moderate fluorescence ($\Phi_F = 0.2-0.3$) with minor phosphorescence ($\Phi_P \sim 10^{-4}$) but exhibits a high ISC quantum yield ($\Phi_{ISC} = 0.7$) and long phosphorescence lifetime ($\tau_p = 0.2$ s) at 77 K.[68−70] One can reasonably expect the ISC rate of $S_{CT1} \rightarrow T_{PP1}$ to reach the picosecond timescale as estimated with an acceptable SOC in this work. Obviously, it is in conflict with the experimentally measured quantum yield of fluorescence, which can be settled by the consideration of the reverse ISC (rISC) due to the ultralong phosphorescence lifetime. We calculated the rate constant of rISC to be 2.1×10^9 to 5.5×10^9 s^{-1} based on the semiclassical Marcus theory.[72,73] Kinetic data analyses show that rISC not only proceeds faster than phosphorescence emission with the second timescale but is predominant over fluorescence emission ($k_F = 9.5 \times 10^7$ s^{-1}), which largely compensates for the quantum yield loss of fluorescence caused by the ultrafast forward ISC. It should be noted that this abnormal dynamic behavior simultaneously promotes the fluorescence emission and the lifetime of the triplet state. Computational results also explain why the performance of thermally activated delayed fluorescence has not been experimentally reported for flavin-based complexes, exhibiting a single fluorescent signal.[66] As shown in Figure 2, 635 nm red phosphorescence can be produced from the minimum of the triplet state, T_{PP1}-Min($^3\pi\pi^*$), along a rapidly falling path, which quantitatively agrees with the experimentally measured emissions peaking at 620 nm with an extremely long lifetime.[68,74] Based on these kinetic data, a conclusion can be drawn that the subsequent EnT and ET events photosensitized by riboflavin dynamically compete with the rate of rISC instead of phosphorescence emission. Most importantly, the visible-light-induced photocatalytic activity of riboflavin emerges gradually along the relaxation path. This can be characterized by increased negative charge around the unsubstituted pyrazinyl N1, i.e., S_0 (−0.57) $\rightarrow S_{CT1}$-Min (−0.63) $\rightarrow T_{PP1}$-Min (−0.67), which eventually becomes an ideal proton acceptor imposing enough extraction capacity on aromatic H for the subsequent catalytic reaction.

$E \rightarrow Z$ Photoisomerization of Cinnamic Acid: Direct Ultraviolet Excitation versus Visible-Light-Driven Photosensitization

The MEPs of $E \rightarrow Z$ photoisomerization of substrate **2** through direct ultraviolet excitation (**3a**) and visible-light-driven photosensitization (**3b**) are illustrated in Figure 3. Upon UV photoexcitation at 297 nm, the isolated *E*-isomer **2** is instantaneously promoted to the FC region of the double bond involved $S_{CT}(^1\pi\pi^*)$ state, originating from the CT excitation along the desired direction of phenyl-centered π to the π^* orbital of C4=C5. The initial decay in the $S_{CT}(^1\pi\pi^*)$ state is characterized structurally by the elongated C4=C5 (1.35 → 1.37 Å) and carbonyl C6=O9 (1.19 → 1.21 Å) bonds accompanied by geometric adjustment of all C−C bonds in the phenyl ring. These structural changes produce a 0.45 eV energy decrease in the $S_{CT}(^1\pi\pi^*)$ state, leading to the conical intersection (CI) of $S_{CT}(^1\pi\pi^*)$/$S_{NP}(^1n\pi^*)$. The relaxation in the $S_{NP}(^1n\pi^*)$ state results in the pyramid deformation of
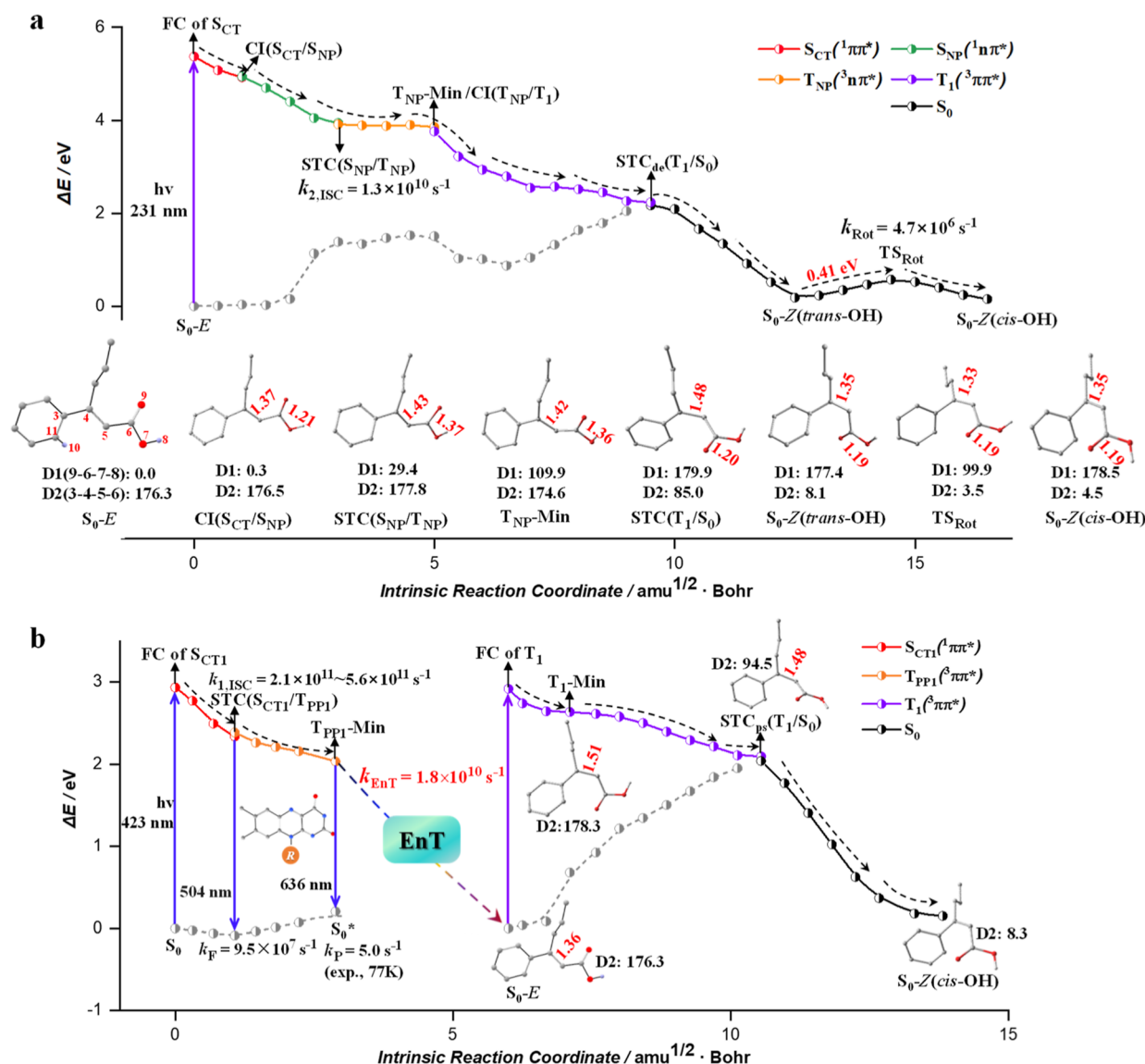
Figure 3. MEPs of the $E \rightarrow Z$ isomerization of **2** via direct ultraviolet excitation (a) and visible-light-driven photosensitized reaction (b). The energy diagram is provided to illustrate the triplet−triplet EnT process from donor **1** in the $T_{PP1}(^3\pi\pi^*)$ state, promoting acceptor **2** to the $T_1(^3\pi\pi^*)$ state. The structural evolutions are shown with selected bond lengths (Å) and dihedral angles (°) along the critical points of the relaxation path. Hydrogen atoms (except H8 of the carbonyl group) were omitted for clarity. The results were obtained in the acetonitrile matrix at the CASPT2// IRC/CASSCF(10e/9o)/PCM level of theory.

carbonyl due to the broken C6═O9 bond, and the system eventually reaches the STC of $S_{NP}(^1n\pi^*)$/$T_{NP}(^3n\pi^*)$ with a ca. 1.00 eV energy decrease. A relatively small SOC (1.6 cm⁻¹) is estimated for the anti-El-Sayed-type $STC(S_{NP}/T_{NP})$ of the isolated substrate **2**, which allows the occurrence of ISC ($k_{2,ISC}$ = 1.3 × 10¹⁰ s⁻¹) with lower efficiency compared to the double bond (STC_{de}-T_1/S_0: 1.48 → S_0-Z: 1.35 Å). It should be noted that the ultraviolet-driven isomerization product, i.e., Z-isomer (trans-OH), is conformationally different from the experimentally measured Z-isomer crystal structure with a counterpart event for catalyst **1** ($k_{1,ISC}$ = 2.1 × 10¹¹ to 5.6 × 10¹¹ s⁻¹).

The following decay in the $T_{NP}(^3n\pi^*)$ state is mainly ascribed to the collapse of the carbonyl π bond, as indicated by the C6═O9 bond length evolution: $CI(S_{CT}/S_{NP})$, 1.20 Å → T_{NP}-Min, 1.36 Å. This further eliminates the rotational restriction of O7−H8 along the C6−O7 bond, for which hydroxyl H8 is eventually located at the opposite side of the carbonyl C6═O9, tending to the generation of a trans-OH

conformer. For instance, the dihedral angle O9−C6−O7−H8 (D1) increases to 109.9° in the minimum of the $^3n\pi^*$ state, T_{NP}-Min($^3n\pi^*$), from the initial 0.0° of the E-isomer. Energy analysis demonstrates that the T_{NP}-Min point energetically matches with the lowest-lying triplet state, i.e., $T_1(^3\pi\pi^*)$, and is therefore denoted as CI of $T_{NP}(^3n\pi^*)$/$T_1(^3\pi\pi^*)$. The decay of isolated **2** in the $T_1(^3\pi\pi^*)$ state gradually exhibits the C4- and C5-centered diradical configuration to release the rotational restriction along the broken double bond, allowing the occurrence of photoisomerization. As shown in Figure 3a, the dihedral angle C3−C4−C5−C6 (D2) decreases to 85.0° in the $^3\pi\pi^*$ state, while it continuously remains unchanged along the relaxation path of the $^{1,3}n\pi^*$ state (D2: ca. 176°). These computational pieces of evidence indicate that the driving force for $E \rightarrow Z$ photoisomerization stems from the population of the double-bond-centered $^3\pi\pi^*$ state with a diradical configuration. Obviously, the n → π* transition of **2** is unlikely to trigger the $E \rightarrow Z$ photoisomerization, although

$n\pi^*$ state decay also leads to the elongation of the C4–C5 bond (>1.40 Å) with single bond character. Similar to the $Z \rightarrow E$ photoisomerization path of retinal,[75,76] the energetically degenerate point of STC_{de} is encountered between the double bond involved T_1 and S_0 states when the planar orientation exhibits a carboxyl plane preferentially perpendicular to the phenyl skeleton (D2: 85.0°). Isolated **2** will thus decay to the S_0 state via this STC_{de} to achieve isomerization, delivering the product of the Z-isomer (*trans*-OH) accompanied by ground-state recovery of double bonds (STC_{de}-T_1/S_0: 1.48 → S_0-Z: 1.35 Å).

It should be noted that the ultraviolet-driven isomerization product, i.e., Z-isomer (*trans*-OH), is conformationally different from the experimentally measured Z-isomer crystal structure with a *cis*-OH conformer.[77,78] A sizable barrier of 0.41 eV (TS_{Rot}) has to be overcome in the ground state to produce the Z-isomer (*cis*-OH), while the OH rotation in the $n\pi^*$ state proceeds smoothly along the barrierless path. Consistently, a low yield (25–30%) was experimentally reported for UV-photogenerated Z-cinnamic acid (*cis*-OH).[79,80]

Considering that direct UV-excited photoisomerization generally suffers from high-energy excitation, low yield of product[79] and the existence of a competitive dimerization channel,[80] substrate **2** tends to follow an indirect excitation via a triplet–triplet energy transfer (EnT). As illustrated in Figure 3b, the visible-light-irradiated photosensitizer **1** decays to the ground state along a nonradiative channel, transferring energy to the E-isomer substrate. Meanwhile, **2** as the energy acceptor is thus directly promoted to the FC region of the $T_1(^3\pi\pi^*)$ state and rapidly decays to its minimum, T_1-Min, which gradually exhibits a diradical character as indicated by C4–C5 moiety-localized singly occupied orbitals and an elongated bond length (1.51 Å) compared with 1.36 Å at FC-$T_1(^3\pi\pi^*)$ and 1.39 Å in the minimum of $S_{CT}(^1\pi\pi^*)$ state. This extremely releases the rotational restriction along the C4–C5 bond at the $T_1(^3\pi\pi^*)$ state to efficiently drive the photosensitized $E \rightarrow Z$ isomerization. Substrate **2** rapidly decays to the STC_{ps} of T_1/S_0 with a perpendicular orientation (D2: 94.5°) to allow the occurrence of rest isomerization in the ground state with the recovery of the double bond, delivering the final product of S_0-Z (*cis*-OH). It should be noted that the $n\pi^*$ state-mediated rotation of O7–H8 along the C6–O7 bond is first triggered, followed by the rotation of the phenyl ring along the C4–C5 bond, causing the dihedral angle of D2 change from 176.3 to 85.0° for the case of direct UV excitation. In contrast to the former case, only the rotation of the phenyl ring is required to achieve the dihedral angle of D2 change from 176.3 to 94.5° along the photosensitized isomerization path in the $\pi\pi^*$ state. Therefore, the carboxyl plane remains unchanged without the involvement of OH rotation in the sensitized isomerization, producing the Z-isomer with *cis*-OH conformation as experimentally measured.[77,78]

Although the adiabatic excitation energy of the donor (2.24 eV) is slightly lower than that of the acceptor (2.56 eV), the criterion of energy matching can be satisfied by consideration of the energy level of vertical excitation between the donor (2.93 eV) and acceptor (2.92 eV). This indicates that the EnT is still operative from excited vibrational or rotational levels of the donor T_{PP1} state without any extra energy input.[30] This case behaves like a typical endergonic EnT to follow Boltzmann kinetics.[30] It is noteworthy that the decay of FC-$S_{CT1}(^1\pi\pi^*) \rightarrow T_{PP1}(^3\pi\pi^*)$-Min for photocatalyst **1** is quite fast

($k_{1,\text{ISC}}$ = 2.1 × 10^{11} 5.6 × 10^{11} s^{-1}) in comparison with excitation energy dissipation through radiative channels (k_F = 9.5 × 10^7 s^{-1}, k_P = 5.0 s^{-1}), producing a high quantum yield of triplet state (0.7 at 77 K).[68,70] This significantly improves the possibility for a population in high energy levels of vibrational and rotational states based on T_{PP1}-Min of the photosensitizer. Therefore, triplet–triplet EnT kinetics are jointly controlled by Boltzmann distribution and the nonradiative EnT rate. Indeed, the quantum efficiency is not high enough within the photocatalytic cycle due to the unfavorable energy level of the donor. This shortcoming can be largely overcome by the high EnT rate and the product accumulation in the repeated cycles of excitation recovery. Consistently, reaction progress monitoring showed that it took ~3 h to complete photosensitized $E \rightarrow Z$ isomerization upon continuous irradiation of the catalytic system.[34]

The theoretical model of triplet–triplet EnT has been established through a short-distance electron exchange mechanism (Scheme 2 and Figure 3b), while the rate

Scheme 2. Schematic Illustration of Dynamic Correlation between EnT and ET Mediated by a Single Photocatalyst[a]
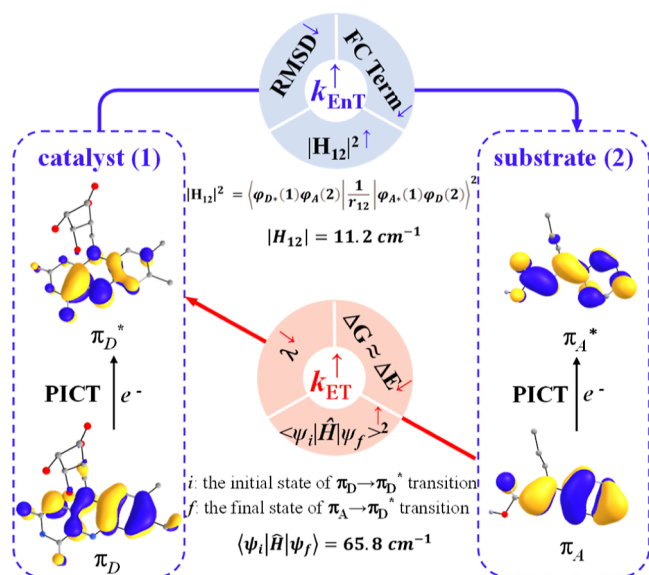
[a]The singly occupied orbitals are schematically shown for the involved excited states together with key parameters. $|H_{12}|$: the electron exchange coupling (EnT) between two electronic states of the donor–acceptor complex, $\langle\psi_i|\hat{H}|\psi_f\rangle$: the electronic coupling (ET) between the initial and final states.

calculations are conducted by using the accurate electronic structures and Fermi's golden rule and summarized in Table 2 together with key parameters. As expected, the EnT rate (k_{EnT}) between photosensitizer **1** and E-isomer **2** was estimated as 1.8 × 10^{10} s^{-1}, which exceeds that of rISC by 1 order and that of phosphorescence emission by 10 orders of magnitude. This kinetic advantage mainly benefits from two favorable factors, the FC and electronic coupling terms. The former one stems from the strong overlap of nuclear wave functions of acceptor **2** between the initial S_0 and the final $T_1(^3\pi\pi^*)$ states, which can be fundamentally attributed to small structural deviation ($RMSD_a$: 0.14) during the S_0-Min → T_1-Min transition. In contrast to the favorable case, a large structural deformation is found in the reverse $Z \rightarrow E$ photosensitized isomerization ($RMSD_a$: 0.88), resulting in an extremely small FC value ($Z \rightarrow$

Table 2. Vertical ($E_{d,ve}$ and $E_{a,ve}$, eV) and Adiabatic ($E_{d,0-0}$ and $E_{a,0-0}$, eV) Excitation Energies Are Summarized for the Donor and Acceptor Together with the Key Parameters of Dexter EnT, Including Root-Mean-Square Deviations during the Transitions of S_0-Min → T_{PP1}-Min for the Donor (−)-Riboflavin (RMSD$_d$, Å) and S_0-Min → T_1-Min for the Acceptor E-Isomer or Z-Isomer (RMSD$_a$, Å), the FC Term (FC, hartree^{-1}), the Electronic Coupling ($|H_{12}|$, cm^{-1}), and the Calculated Rates (k_{EnT}, s^{-1})

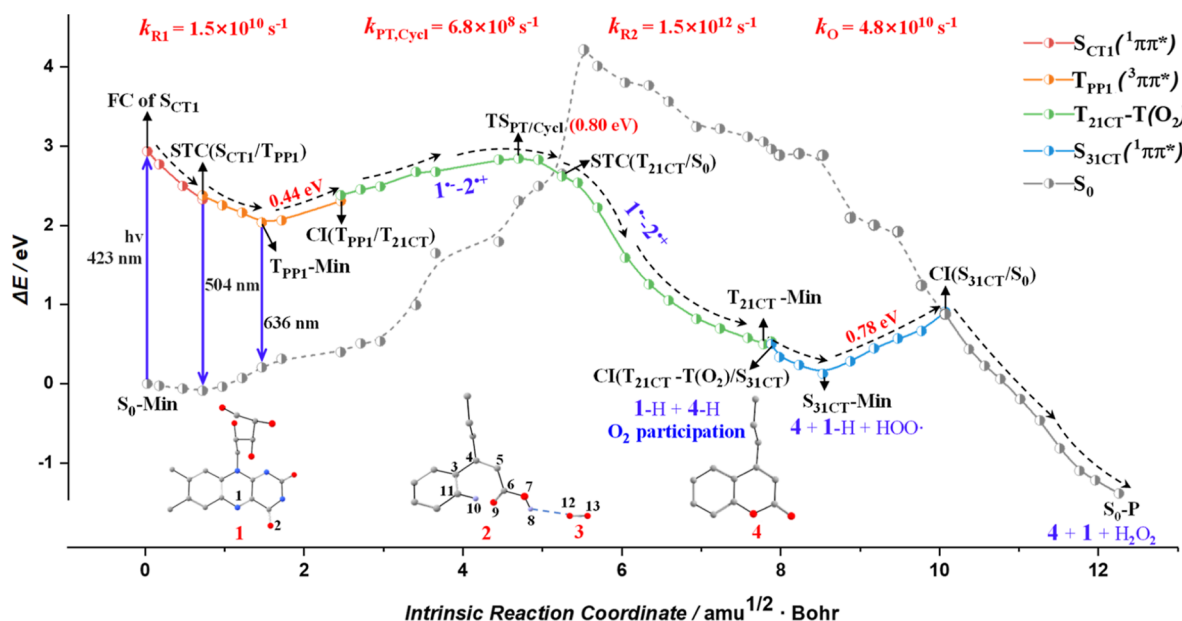| acceptor	$E_{d,ve}$	$E_{d,0-0}$	$E_{a,ve}$	$E_{a,0-0}$	RMSD$_d$	RMSD$_a$	FC	$|H_{12}|$	k_{EnT}
E-isomer	2.93	2.24	2.92	2.56	0.06	0.14	26.0	11.2	1.8×10^{10}
Z-isomer	2.93	2.24	3.67	2.64	0.06	0.88	2.4×10^{-8}	76.0	7.4×10^2

Figure 4. MEPs of SET events in the reductive quenching cycle for the photoinduced PCET and PT-coupled aromatic C−H functionalization/cyclization through the asynchronous concerted mechanism. The barrier of TS$_{PT/Cycl}$ is defined to compare with the T$_{PP1}$-Min. The hydrogen atoms (except H8 and H10) were omitted for clarity. The results were obtained in the acetonitrile matrix at the CASPT2//IRC/CASSCF/PCM level of theory, and the kinetic data are also provided.

Scheme 3. Dual-Nonadiabatic-Crossing SET Model Integrated with the Rate-Determining Transition State (TS$_{PT/Cycl}$) Is Schematically Shown together with Their Key Kinetic Parameters along the Asynchronous Concerted Path
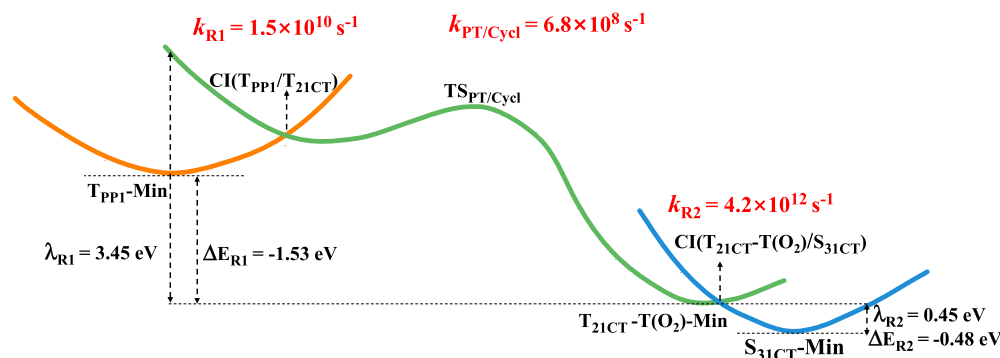
E: 2.4×10^{-8} hartree^{-1} vs $E \to Z$: 26.0 hartree^{-1}). Another dynamic controlling factor refers to the term electronic coupling, which originates from the overlap of involved orbitals in the electron exchange process. As shown in Scheme 2, electron exchange for EnT of **1−2** complex takes place between the π_D/π_D^* orbitals of **1** and π_A/π_A^* orbitals of **2**. Moreover, these involved orbitals exactly account for the singly occupied orbitals for the T$_{PP1}$($^3\pi\pi^*$) state of donor **1** and T$_1$($^3\pi\pi^*$) state of acceptor **2**, i.e., the initial and final states of triplet−triplet EnT, exhibiting similar CT features. Benefiting from the similarity of electron transition, an acceptable

coupling term (11.2 cm^{-1}) was calculated for the $E \to Z$ photosensitized isomerization, while this value increased to 76.0 cm^{-1} for the reverse $Z \to E$ photoisomerization due to enhanced PICT of the T$_1$($^3\pi\pi^*$) state in case of the collapse of the conjugated plane for the Z-isomer acceptor. However, the intensive coupling is unlikely to significantly improve the EnT rate (7.4×10^2 s^{-1}) for the reverse one, which is the result of the negligible FC term and essentially stems from an inaccessibly energetic level for the Z-isomer acceptor in the triplet state (A: 3.67 eV vs D: 2.93 eV). The present kinetic data explain why the high-energy Z-isomer becomes
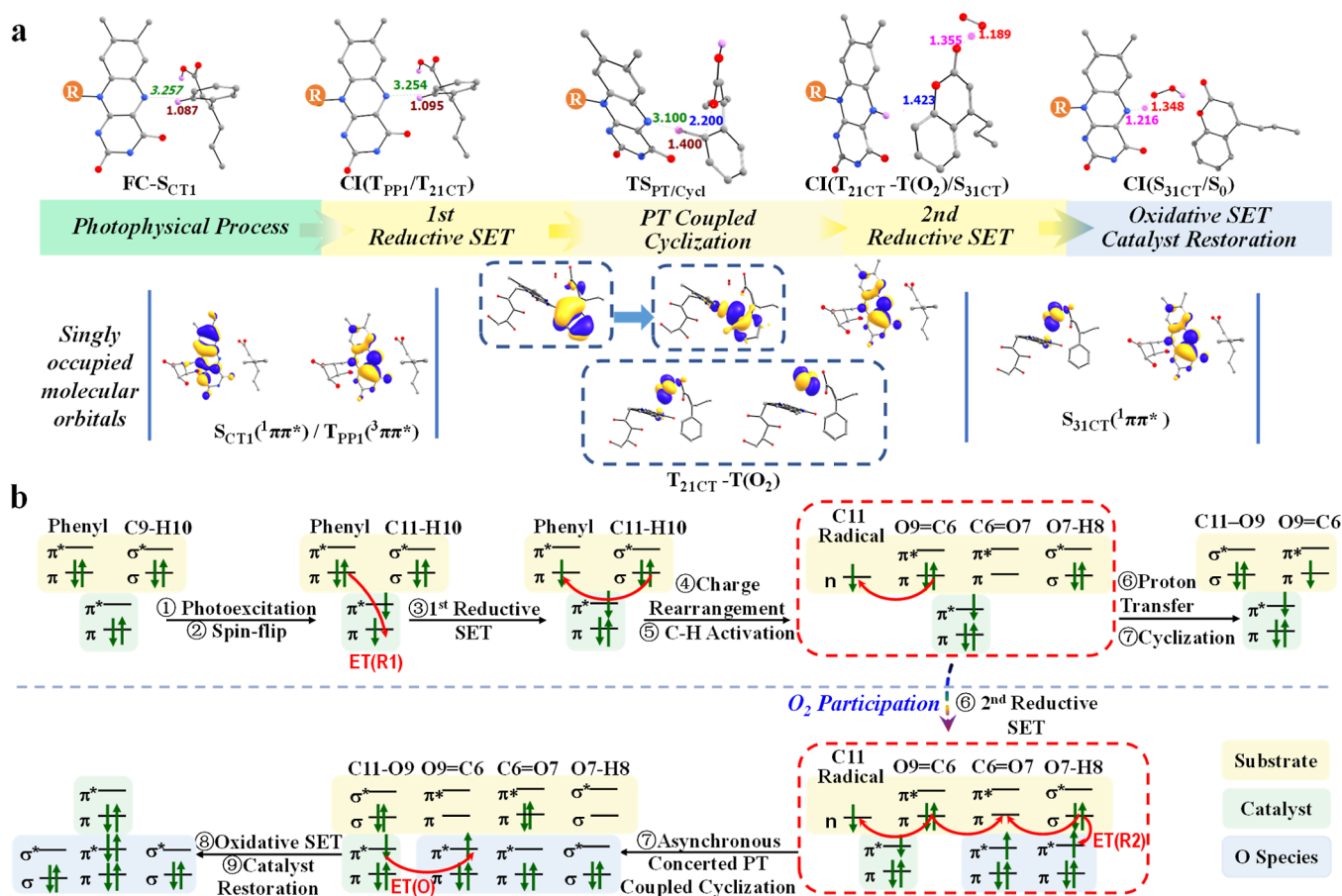
Figure 5. (a) Structural evolutions along the critical points of relaxation paths with their key bond distances (Å) and the evolution of singly occupied orbitals in the reductive quenching cycle for the photoinduced PCET and PT-coupled aromatic C−H functionalization/cyclization. (b) Electron shifts among the involved orbitals in the catalytic cycle.

predominant over the *E*-isomer in the presence of a visible-light-irradiated photosensitizer,[33] showing an anti-Boltzmann behavior.

Photoinduced Proton-Coupled ET and Proton Transfer-Coupled Aromatic C−H Functionalization/Cyclization

Besides the dynamic advantage of the EnT, photocatalyst **1** is capable of simultaneously and effectively catalyzing aromatic C−H functionalization/cyclization via a SET path. To obtain the dynamic information of SET, the MEPs of SET-driven proton transfer (PT) and cyclization have been mapped by accurate electronic structure calculations in the acetonitrile matrix at the CASPT2//IRC/CASSCF/PCM level of theory and shown in Figure 4, while the established SET models are provided together with their key parameters in Scheme 3 by using the Marcus theory of ET. In the presence of the Z-isomer substrate **2**, a strong C11−H10⋯N1 intermolecular hydrogen bond is formed between **1** and **2** and undergoes further enhancement from 2.22 Å (FC-S$_{CT1}$) to 2.21 Å (T$_{PP1}$-Min) in the relaxation process of the visible-irradiated photocatalyst due to the accumulation of the photoinduced negative charge around N1. These tiny reorganizations of the complex structure are not trivial but trigger the preliminary activation of the aromatic C11−H10 bond (S$_0$: 1.08 Å → 1.09 Å), which promotes **1**−**2** complex reaching CI between the T$_{PP1}$($^3\pi\pi^*$) precursor state and the reduction state of **1** denoted as T$_{21CT}$($^3\pi\pi^*$). In this process, a moderate barrier of 0.44 eV

requires to be overcome and thus allows the occurrence of reductive SET from the π_A orbital of substrate **2** to the π_D^* orbital of photocatalyst **1** (see Scheme 2). The zwitterionic complex of **1**$^{•−}$-**2**$^{•+}$ is generated to exhibit a remarkable increase of dipole moment (T$_{PP1}$: 13.6 Debye → T$_{21CT}$: 21.6 Debye), accompanied by the enforced C11−H10⋯N1 hydrogen bond and the further activation of the inert C11−H10 bond (Figure 5).

Mulliken population analysis demonstrates that the ejected electron from substrate **2** mainly distributes in the pyrazinyl moiety of **1**$^{•−}$, which imposes strong attraction on the opposite H10 of **2**$^{•+}$ via the enhanced interaction of the C11−H10⋯N1 hydrogen bond. Based on favorable charge redistribution, the H10 deviation proceeds as a manner of PT approaching N1. In this process, the energy consumption of C11−H10 bond dissociation is largely compensated by the N1−H10 formation, which allows the catalytic reaction to occur along an energy-saving PT path. Numerous computational tests demonstrate that the lower bound of the PT barrier (see Figure S6) is estimated to be 3.46 eV (358 nm) relative to the zero level of S$_0$-Min and 0.53 eV higher than FC-S$_{CT1}$, beyond the visible spectral range. Therefore, an extra kinetic factor has to be taken to couple with the PT process for driving inert C−H functionalization. For favorable consideration, when the C11−H10 distance increases to a certain length (i.e., >1.3 Å) the partially exposed C11$^•$ radical tends to attack the O9 of carbonyl, causing a significant energy decrease of the triplet state (see Figure 4). Following this clue, the transition state for

the asynchronous concerted mechanism, donated as $TS_{PT/Cycl}$, was determined to dynamically dominate the coupled PT and cyclization processes. In this case, the released energies of N1−H10 bond formation and cyclization jointly promote the realization of aromatic C−H functionalization, in which the barrier of $TS_{PT/Cycl}$ for the coupled PT/cyclization processes decreases to an acceptable value (0.80 eV relative to the zero level of T_{PP1}-Min) compared with that of the individual PT reaction (1.43 eV, see Figure S6). It is worth noting that the energy consumption (2.84 eV relative to the zero level of S_0-Min) for catalytic aromatic C−H bond cleavage coupled with cyclization is lower than the input loading by visible-light irradiation and ∼40% reduced compared with that of bond dissociation energy (BDE: 4.77−5.12 eV).[35] This fundamentally benefits from the adopted proton-coupled ET (PCET) mechanism,[81−85] in which the ejected electron in photocatalyst **1** drives the proton departure from substrate **2** to exhibit two spatially and temporally separated SET and PT processes with kinetic correlation. After surmounting the $TS_{PT/Cycl}$, an STC between the T_{21CT} and S_0 states is encountered due to the rapid ascend of the energetic level of the ground state. The rising energy of S_0 eventually surpasses the energy curve of the triplet state with a gradually increasing energy gap (up to 2.47 eV), which essentially acts as a functional hindrance to block the reverse SET via the $T_{21CT} \rightarrow S_0$ state. As discussed in our previous work,[47] the existence of functional hindrance extremely reduces the rate of the reverse SET to ensure the efficiency of the PT-coupled cyclization reaction.

The subsequent PT-coupled cyclization proceeds smoothly along a downhill pathway and relaxes to the minimum of the T_{21CT} state (T_{21CT}-Min), i.e., a neutral hydrogenated catalyst (**1**-H) and the preliminary product of the hydrogenated hexatomic heterocycle (**4**-H). Qualitatively, an extra oxidant such as O_2 (**3**) is required to participate in the reductive SET, by which the excess electron localized in the heterocycle-centered π^* orbital of **4**-H can be switched to the π^* orbital of **3**, generating the reductive singlet state, i.e., S_{31CT} (**4**$^+$-H-O_2^-). The compatibility of the O_2 participation was inspected and confirmed by the energetically matched paths in the absence and presence of O_2 (see Figure S7). As expected, one more nonadiabatic crossing of $CI(T_{21CT}$-$T(O_2)/S_{31CT})$ is encountered when the catalytic system just moves out of the minimum region of the T_{21CT} state. This funnels them toward the minimum structure of the S_{31CT} state, i.e., S_{31CT}-Min, to accomplish the second reductive SET. In this case, SET-driven PT (PCET) takes place once again imposed by the strong attraction of O_2^- on the proton H8, delivering the final product **4** with the formation of a carbonyl in the heterocycle. Overall, triplet oxygen is a strong electron acceptor, which readily captures the electron of the hexatomic heterocycle-centered radical (**4**$^-$-H) to form O_2^- with stronger electronegativity. The generated O_2^- subsequently triggers a rapid PT to deliver **4**$^+$-H into the final product following an energy-saving PCET path. Meanwhile, the generated HOO$^\bullet$ acts as an ideal H acceptor to realize the recovery of the catalyst driven by oxidative SET via a PCET mechanism. However, a middle-size barrier (0.78 eV) is found due to the energy consumption of N−H activation (H atom deviation: 1.00 → 1.22 Å) to promote the catalytic system reaching the CI of $S_{31CT}(^1\pi\pi^*)/S_0$. With the electron repopulation in HOO$^\bullet$, the movement of proton H10 takes place easily along a downhill PCET path, achieving catalyst recovery and the generation of hydrogen peroxide.

Extended SET Model of Transition-State-Coupled Dual-Nonadiabatic Crossings with Its Kinetic Evaluation and the Dynamic Correlation with EnT

An extended SET model has been developed to integrate the Marcus ET with the transition-state theory (TST), which can be used to disclose the inherent driving force for the multifactorial control of PT-coupled cyclization. As shown in Scheme 3, the aromatic C−H functionalization/cyclization reaction is dynamically characterized by the dual-nonadiabatic crossings of $CI(T_{PP1}/T_{21CT})$ and $CI(T_{21CT}$-$T(O_2)/S_{31CT})$ integrated with the transition state ($TS_{PT/Cycl}$) for the PT-coupled cyclization. Although the reorganization energy of the first reductive SET is quite high (λ_{R1} = 3.45 eV), other two favorable parameters, i.e., the electron coupling (65.8 cm^{-1}) and the Gibbs free energy change (approximately equal to ΔE_{R1}, −1.53 eV), have been found to stem from the similar electron transition character (CT) for the involved initial (T_{PP1}) and final (T_{21CT}) states and the high-exothermic PT-coupled cyclization (>2.0 eV), respectively. From balance considerations, these physical parameters allow the first reductive SET-associated nonadiabatic transition from T_{PP1} to T_{21CT} to take place effectively (k_{R1} = 1.5 × 10^{10} s^{-1}).

Based on the barrier of $TS_{PT/Cycl}$, the rate of the asynchronous concerted PT-coupled cyclization reaction can be estimated as 2.2 × 10^8 s^{-1} by using TST with consideration of free energy correction in acetonitrile solvent. Thus, a relatively fast k_{R1} not only predominates over the rISC ($k_{1,rISC}$ = 2.1 × 10^9 to 5.5 × 10^9 s^{-1}) and the radiative relaxation of the photocatalyst (τ_P = 0.2 s at 77 K)[68] but makes ET faster than PT by 2 orders of magnitude, exhibiting a typical PCET behavior. It is worth noting that in the present case, the proton migration is unlikely to be a standalone dynamic process but correlates with the structural reorganization of cyclization. These kinetic data demonstrate that the rate-determining step of $TS_{PT/Cycl}$ is correlatedly controlled by combined multiple dynamic models of SET, PT, and cyclization, which still behaves as in the case of a slow proton/fast electron as the PCET mechanism. The dynamic complexity of the extended SET model further originates from the appended factor of the second reductive SET in the presence of an O_2 quencher for the oxidative state of the substrate. The second reductive SET (k_{R2} = 4.2 × 10^{12} s^{-1}) via the CI of T_{21CT}-$T(O_2)/S_{31CT}$ takes place more effectively than the first one and the PT-coupled cyclization due to the relatively small reorganization energy (0.45 eV) and the strong electron coupling (106 cm^{-1}). From dynamic considerations, in the present case, the second reductive SET imposes a negligible impact on the rate-determining step of $TS_{PT/Cycl}$ since they are separated spatially temporally and approach the decoupling behavior. In some special cases, the rate-determining TS may strongly correlate with dual ET processes to extremely enhance dynamic complexity, which will guide the experimental chemists to design more complex photochemistry transformations by using tunable parameters.

Collected evidence from Gilmour's experiment investigation demonstrates that the substrate (*E*-isomer), intermediate (*Z*-isomer), and product can be observed simultaneously within 1−3 h via reaction progress monitoring, while the complete *E*-isomer substrate totally disappears over the course of 3 h.[34] This indicates that EnT and ET mechanisms are operated in concert instead of two processes combined classically, exhibiting high dynamic correlation. Herein, the advantages of electronic structure and excited states would be analyzed to

disclose why photocatalyst **1** can function as both EnT and ET photosensitizers in the dynamically correlated processes. First, the coupling terms for nonadiabatic interaction (ET) and electron exchange (EnT) are quite large, which can be attributed to the similarities in character of the transition states (PICT) and properties of the involved orbitals for photocatalyst **1** and substrate **2** (see Scheme 2). Second, flavin derivatives essentially act as the optimal photosensitizers since they exhibit small RMSD values during the repeated cycles of excitation and recovery and ultralong triplet-state lifetime, providing a wide time window for subsequent photosensitized EnT and ET reactions. Finally, energy is an important aspect to be considered: the high-energy donor could accelerate the EnT rate through an increased FC term under the condition of energy matching, while the ideal photosensitizers are liable to catalytically activate highly exothermic ET reactions for the proposed SET model in this work.

CONCLUSIONS

The dynamically associated EnT and ET paths were mapped for (−)-riboflavin-photocatalyzed cascade reactions of isomerization and cyclization by using accurate electronic structure calculations at the CASPT2//CASSCF/PCM level of theory. The highly effective $E \rightarrow Z$ photoisomerization of the cinnamic acid derivative was theoretically rationalized by the triplet–triplet EnT mechanism using Fermi's golden rule and the Dexter model. An extended SET model has been developed to integrate the Marcus ET with TST, i.e., the dual-nonadiabatic crossings coupled with the rate-determining transition state, which can be used to account for the dynamic behaviors and kinetic assessments of the ET-driven aromatic C−H functionalization. Kinetic data demonstrate that the high yield of the isomerization product is largely ascribed to the rigidity of the substrate and photosensitizer, the strong electron exchange coupling, and the large FC term. Besides these favorable dynamic parameters, the dual-functional photosensitizer also contributes to the considerable electron coupling and free energy reduction for the highly exothermic PT-coupled cyclization. Based on the innovative SET model, catalytic aromatic C−H functionalization was verified to be correlatedly controlled by combined multiple dynamic processes, such as the reductive SET, PT-coupled cyclization, and catalyst restoration via O_2 quenching along an energy-saving path. These computational insights provide abundant dynamic and kinetic information to help understand the mechanism and driving force of aromatic C−H functionalization/cyclization jointly controlled by EnT and ET, which will facilitate the mechanism-guided molecular design of dual-functional photosensitizers and innovative photocatalytic reactions with multiple activation modes..

ASSOCIATED CONTENT

ⓢ Supporting Information

The Supporting Information is available free of charge at https://pubs.acs.org/doi/10.1021/jacsau.3c00098.

> Computational details on CASPT2//CASSCF, rate constant calculations, fluorescence-emission rate calculations, calculations of vertical excitation and adiabatic excitation for the substrate, aromatic C−H bond functionalization reaction and the backward $Z \rightarrow E$ isomerization, physical and geometric parameters,

Cartesian coordinates of critical points, and additional references (PDF)

AUTHOR INFORMATION

Corresponding Authors

Juanjuan Wang − *College of Nuclear Science and Technology, Beijing Normal University, Beijing 100875, China; Laboratory of Beam Technology and Energy Materials, Advanced Institute of Natural Science, Beijing Normal University, Zhuhai 519087, China*; Email: jjwang@bnu.edu.cn

Xuebo Chen − *Department of Chemistry, Beijing Normal University, Beijing 100875, China;* ⓘ orcid.org/0000-0002-9814-9908; Email: xuebochen@bnu.edu.cn

Authors

Xiaorui Zhang − *Department of Chemistry, Beijing Normal University, Beijing 100875, China*

Lin Liu − *Department of Chemistry, Beijing Normal University, Beijing 100875, China*

Weijia Li − *Department of Chemistry, Beijing Normal University, Beijing 100875, China*

Chu Wang − *Department of Chemistry, Beijing Normal University, Beijing 100875, China*

Wei-Hai Fang − *Department of Chemistry, Beijing Normal University, Beijing 100875, China;* ⓘ orcid.org/0000-0002-1668-465X

Complete contact information is available at:
https://pubs.acs.org/10.1021/jacsau.3c00098

Notes

The authors declare no competing financial interest.

REFERENCES

(1) Jacobsen, E. N.; MacMillan, D. W. C. Organocatalysis. *Proc. Natl. Acad. Sci. U.S.A.* **2010**, *107*, 20618−20619.

(2) List, B. Introduction: Organocatalysis. *Chem. Rev.* **2007**, *107*, 5413−5415.

(3) Holland, M. C.; Gilmour, R. Deconstructing Covalent Organocatalysis. *Angew. Chem., Int. Ed. Engl.* **2015**, *54*, 3862−3871.

(4) von Liebig, J. Ueber die Bildung des Oxamids aus Cyan. *Justus Liebigs Ann. Chem.* **1860**, *113*, 246−247.

(5) List, B.; Lerner, R. A.; Barbas, C. F. Proline-Catalyzed Direct Asymmetric Aldol Reactions. *J. Am. Chem. Soc.* **2000**, *122*, 2395−2396.

(6) Ahrendt, K. A.; Borths, C. J.; MacMillan, D. W. C. New Strategies for Organic Catalysis: The First Highly Enantioselective Organocatalytic Diels-Alder Reaction. *J. Am. Chem. Soc.* **2000**, *122*, 4243−4244.

(7) MacMillan, D. W. C. The Advent and Development of Organocatalysis. *Nature* **2008**, *455*, 304−308.

(8) Bugaut, X.; Glorius, F. Organocatalytic Umpolung: N-Heterocyclic Carbenes and Beyond. *Chem. Soc. Rev.* **2012**, *41*, 3511−3522.

(9) Pellissier, H. Recent Developments in Asymmetric Organocatalytic Domino Reactions. *Adv. Synth. Catal.* **2012**, *354*, 237−294.

(10) Oliveira, V.; Cardoso, M.; Forezi, L. Organocatalysis: A Brief Overview on Its Evolution and Applications. *Catalysts* **2018**, *8*, 605.

(11) Oxtoby, L. J.; Li, Z.-Q.; Tran, V. T.; Erbay, T. G.; Deng, R.; Liu, P.; Engle, K. M. A Transient-Directing-Group Strategy Enables Enantioselective Reductive Heck Hydroarylation of Alkenes. *Angew. Chem., Int. Ed. Engl.* **2020**, *59*, 8885−8890.

(12) Basavaiah, D.; Sharada, D. S.; Veerendhar, A. Organo-base Mediated Cannizzaro Reaction. *Tetrahedron Lett.* **2006**, *47*, 5771−5774.

(13) Zoller, B.; Stach, T.; Huy, P. H. Lewis Base Catalysis Enables the Activation of Alcohols by Means of Chloroformates as Phosgene Substitutes. *ChemCatChem* **2020**, *12*, 5637−5643.

(14) Tanimoto, K.; Okai, H.; Oka, M.; Ohkado, R.; Iida, H. Aerobic Oxidative C-H Azolation of Indoles and One-Pot Synthesis of Azolyl Thioindoles by Flavin-Iodine-Coupled Organocatalysis. *Org. Lett.* **2021**, *23*, 2084−2088.

(15) Foster, R. S.; Adams, H.; Jakobi, H.; Harrity, J. P. Synthesis of 4-Fluoromethylsydnones and Their Participation in Alkyne Cyclo-addition Reactions. *J. Org. Chem.* **2013**, *78*, 4049−4064.

(16) Browne, D. L.; Taylor, J. B.; Plant, A.; Harrity, J. P. Alkyne [3 + 2] Cycloadditions of Iodosydnones Toward Functionalized 1,3,5-Trisubstituted Pyrazoles. *J. Org. Chem.* **2010**, *75*, 984−987.

(17) Weinbender, T.; Hofmann, M.; Reiser, O. Functional Changes of Biomolecules and Organocatalysts as a Probe for Pressure Effects in Solution. *Biophys. Chem.* **2020**, *257*, 106280.

(18) Kristofikova, D.; Modrocka, V.; Meciarova, M.; Sebesta, R. Green Asymmetric Organocatalysis. *ChemSusChem* **2020**, *13*, 2828−2858.

(19) Beeson, T. D.; Mastracchio, A.; Hong, J. B.; Ashton, K.; MacMillan, D. W. C. Enantioselective Organocatalysis Using SOMO Activation. *Science* **2007**, *316*, 582−585.

(20) Jang, H. Y.; Hong, J. B.; MacMillan, D. W. C. Enantioselective Organocatalytic Singly Occupied Molecular Orbital Activation: The Enantioselective α-Enolation of Aldehydes. *J. Am. Chem. Soc.* **2007**, *129*, 7004−7005.

(21) Kim, H.; MacMillan, D. W. C. Enantioselective Organo-SOMO Catalysis: The α-Vinylation of Aldehydes. *J. Am. Chem. Soc.* **2008**, *130*, 398−399.

(22) Mukherjee, S.; List, B. Radical Catalysis. *Nature* **2007**, *447*, 152−153.

(23) MacMillan, D. W. C.; Beeson, T. D. SOMO and Radical Chemistry in Organocatalysis. In *Asymmetric Organocatalysis 1*; List, B., Ed.; Wiley: Stuttgart, Germany, 2012; Vol. *1*, pp 271−307.

(24) Nicewicz, D. A.; MacMillan, D. W. C. Merging Photoredox Catalysis with Organocatalysis: The Direct Asymmetric Alkylation of Aldehydes. *Science* **2008**, *322*, 77−80.

(25) Arceo, E.; Montroni, E.; Melchiorre, P. Photo-Organocatalysis of Atom-Transfer Radical Additions to Alkenes. *Angew. Chem., Int. Ed. Engl.* **2014**, *53*, 12064−12068.

(26) Romero, N. A.; Nicewicz, D. A. Organic Photoredox Catalysis. *Chem. Rev.* **2016**, *116*, 10075−10166.

(27) Kozlowski, M.; Yoon, T. Editorial for the Special Issue on Photocatalysis. *J. Org. Chem.* **2016**, *81*, 6895−6897.

(28) Zhou, Q. Q.; Zou, Y. Q.; Lu, L. Q.; Xiao, W. J. Visible-Light-Induced Organic Photochemical Reactions through Energy-Transfer Pathways. *Angew. Chem., Int. Ed. Engl.* **2019**, *58*, 1586−1604.

(29) Tanner, P. A.; Zhou, L.; Duan, C.; Wong, K. L. Misconceptions in Electronic Energy Transfer: Bridging the Gap between Chemistry and Physics. *Chem. Soc. Rev.* **2018**, *47*, 5234−5265.

(30) Strieth-Kalthoff, F.; James, M. J.; Teders, M.; Pitzer, L.; Glorius, F. Energy Transfer Catalysis Mediated by Visible Light: Principles, Applications, Directions. *Chem. Soc. Rev.* **2018**, *47*, 7190−7202.

(31) Strieth-Kalthoff, F.; Glorius, F. Triplet Energy Transfer Photocatalysis: Unlocking the Next Level. *Chem* **2020**, *6*, 1888−1903.

(32) Chen, J. R.; Yan, D. M.; Wei, Q.; Xiao, W. J. Photocascade Catalysis: A New Strategy for Cascade Reactions. *ChemPhotoChem* **2017**, *1*, 148−158.

(33) Metternich, J. B.; Gilmour, R. A Bio-Inspired, Catalytic E → Z Isomerization of Activated Olefins. *J. Am. Chem. Soc.* **2015**, *137*, 11254−11257.

(34) Metternich, J. B.; Gilmour, R. One Photocatalyst, n Activation Modes Strategy for Cascade Catalysis: Emulating Coumarin Biosynthesis with (-)-Riboflavin. *J. Am. Chem. Soc.* **2016**, *138*, 1040−1045.

(35) Qin, Y.; Zhu, L.; Luo, S. Organocatalysis in Inert C-H Bond Functionalization. *Chem. Rev.* **2017**, *117*, 9433−9520.

(36) Dutta, U.; Maiti, S.; Bhattacharya, T.; Maiti, D. Arene Diversification through Distal C(sp^2)-H Functionalization. *Science* **2021**, *372*, 701.

(37) Wedi, P.; van Gemmeren, M. Arene-Limited Nondirected C-H Activation of Arenes. *Angew. Chem., Int. Ed. Engl.* **2018**, *57*, 13016−13027.

(38) Hari, D. P.; Schroll, P.; Konig, B. Metal-Free, Visible-Light-Mediated Direct C-H Arylation of Heteroarenes with Aryl Diazonium Salts. *J. Am. Chem. Soc.* **2012**, *134*, 2958−2961.

(39) Marzo, L.; Ghosh, I.; Esteban, F.; König, B. Metal-Free Photocatalyzed Cross Coupling of Bromoheteroarenes with Pyrroles. *ACS Catal.* **2016**, *6*, 6780−6784.

(40) Ghosh, I.; Ghosh, T.; Bardagi, J. I.; Konig, B. Reduction of Aryl Halides by Consecutive Visible Light-Induced Electron Transfer Processes. *Science* **2014**, *346*, 725−728.

(41) König, B.; Kümmel, S.; Svobodová, E.; Cibulka, R. Flavin Photocatalysis. *Phys. Sci. Rev.* **2018**, *3*, 20170168.

(42) Mojr, V.; Svobodova, E.; Strakova, K.; Nevesely, T.; Chudoba, J.; Dvorakova, H.; Cibulka, R. Tailoring Flavins for Visible Light Photocatalysis: Organocatalytic [2+2] Cycloadditions Mediated by a Flavin Derivative and Visible Light. *Chem. Commun.* **2015**, *51*, 12036−12039.

(43) Sideri, I. K.; Voutyritsa, E.; Kokotos, C. G. Photo-organocatalysis, Small Organic Molecules and Light in the Service of Organic Synthesis: the Awakening of a Sleeping Giant. *Org. Biomol. Chem.* **2018**, *16*, 4596−4614.

(44) Shaw, M. H.; Twilton, J.; MacMillan, D. W. Photoredox Catalysis in Organic Chemistry. *J. Org. Chem.* **2016**, *81*, 6898−6926.

(45) Ma, L.; Fang, W. H.; Shen, L.; Chen, X. Regulatory Mechanism and Kinetic Assessment of Energy Transfer Catalysis Mediated by Visible Light. *ACS Catal.* **2019**, *9*, 3672−3684.

(46) Yang, W.; Chen, X.; Fang, W. Nonadiabatic Curve-Crossing Model for the Visible-Light Photoredox Catalytic Generation of Radical Intermediate via a Concerted Mechanism. *ACS Catal.* **2018**, *8*, 7388−7396.

(47) Wang, J.; Fang, W. H.; Qu, L. B.; Shen, L.; Maseras, F.; Chen, X. An Expanded SET Model Associated with the Functional Hindrance Dominates the Amide-Directed Distal sp^3 C-H Function-alization. *J. Am. Chem. Soc.* **2021**, *143*, 19406−19416.

(48) Marcus, R. A. Chemical and Electrochemical Electron-Transfer Theory. *Annu. Rev. Phys. Chem.* **1964**, *15*, 155−196.

(49) Marcus, R. A.; Sutin, N. Electron transfers in chemistry and biology. *Biochim. Biophys. Acta Rev. Bioenerg.* **1985**, *811*, 265−322.

(50) Marcus, R. A. Electron Transfer Reactions in Chemistry. Theory and Experiment. *Angew. Chem., Int. Ed.* **1993**, *32*, 1111−1121.

(51) Marcus, R. A. Transfer Reactions in Chemistry. Theory and Experiment. *Pure Appl. Chem.* **1997**, *69*, 13−29.

(52) Cave, R. J.; Newton, M. D. Generalization of the Mulliken-Hush Treatment for the Calculation of Electron Transfer Matrix Elements. *Chem. Phys. Lett.* **1996**, *249*, 15−19.

(53) Cave, R. J.; Newton, M. D. Calculation of Electronic Coupling Matrix Elements for Ground and Excited State Electron Transfer Reactions: Comparison of the Generalized Mulliken-Hush and Block Diagonalization Methods. *J. Chem. Phys.* **1997**, *106*, 9213−9226.

(54) Van Voorhis, T.; Kowalczyk, T.; Kaduk, B.; Wang, L. P.; Cheng, C. L.; Wu, Q. The Diabatic Picture of Electron Transfer, Reaction Barriers, and Molecular Dynamics. *Annu. Rev. Phys. Chem.* **2010**, *61*, 149−170.

(55) Malmqvist, P. Å. Calculation of transition density matrices by nonunitary orbital transformations. *Int. J. Quantum Chem.* **1986**, *30*, 479−494.

(56) Malmqvist, P.-A.; Roos, B. O. The CASSCF State Interaction Method. *Chem. Phys. Lett.* **1989**, *155*, 189−194.

(57) Garrett, B. C.; Truhlar, D. G. Generalized transition state theory. Bond energy-bond order method for canonical variational calculations with application to hydrogen atom transfer reactions. *J. Am. Chem. Soc.* **1979**, *101*, 4534−4548.

(58) Truhlar, D. G.; Hase, W. L.; Hynes, J. T. Current Status of Transition State Theory. *J. Phys. Chem.* **1983**, *87*, 2664−2682.

(59) Garrett, B. C.; Truhlar, D. G. Variational Transition State Theory. Primary Kinetic Isotope Effects for Atom Transfer Reactions. *J. Am. Chem. Soc.* **1980**, *102*, 2559−2570.

(60) Vande Linde, S. R.; Mondro, S. L.; Hase, W. L. Transition States and Rate Constants for Ion−Molecule Association. II. $Li^+(CH_3)_2O \rightarrow Li^+[(CH_3)_2O]$. *J. Chem. Phys.* **1987**, *86*, 1348−1355.

(61) Lin, S. H.; Xiao, W. Z.; Dietz, W. Generalized Forster-Dexter Theory of Photoinduced Intramolecular Energy Transfer. *Phys. Rev. E: Stat. Phys., Plasmas, Fluids, Relat. Interdiscip. Top.* **1993**, *47*, 3698−3706.

(62) Dexter, D. L. A Theory of Sensitized Luminescence in Solids. *J. Chem. Phys.* **1953**, *21*, 836−850.

(63) Han, J.; Shen, L.; Chen, X.; Fang, W. Phosphorescent Mechanism for Single-Dopant White OLED of FPt: Electronic Structure and Electron Exchange-Induced Energy Transfer. *J. Mater. Chem. C* **2013**, *1*, 4227−4235.

(64) Frisch, M. J.; Trucks, G. W.; Schlegel, H. B.; Scuseria, G. E.; Robb, M. A.; Cheeseman, J. R.; Scalmani, G.; Barone, V.; Petersson, G. A.; Nakatsuji, H.; Li, X.; Caricato, M.; Marenich, A. V.; Bloino, J.; Janesko, B. G.; Gomperts, R.; Mennucci, B.; Hratchian, H. P.; Ortiz, J. V.; Izmaylov, A. F.; Sonnenberg, J. L.; Williams-Young, D.; Ding, F.; Lipparini, F.; Egidi, F.; Goings, J.; Peng, B.; Petrone, A.; Henderson, T.; Ranasinghe, D.; Zakrzewski, V. G.; Gao, J.; Rega, N.; Zheng, G.; Liang, W.; Hada, M.; Ehara, M.; Toyota, K.; Fukuda, R.; Hasegawa, J.; Ishida, M.; Nakajima, T.; Honda, Y.; Kitao, O.; Nakai, H.; Vreven, T.; Throssell, K.; Montgomery, J. A.; Peralta, J. E.; Ogliaro, F.; Bearpark, M. J.; Heyd, J. J.; Brothers, E. N.; Kudin, K. N.; Staroverov, V. N.; Keith, T. A.; Kobayashi, R.; Normand, J.; Raghavachari, K.; Rendell, A. P.; Burant, J. C.; Iyengar, S. S.; Tomasi, J.; Cossi, M.; Millam, J. M.; Klene, M.; Adamo, C.; Cammi, R.; Ochterski, J. W.; Martin, R. L.; Morokuma, K.; Farkas, O.; Foresman, J. B.; Fox, D. J. *Gaussian 16*, Revision C.01; Gaussian, Inc.: Wallingford CT, 2016.

(65) Karlström, G.; Lindh, R.; Malmqvist, P.-Å.; Roos, B. O.; Ryde, U.; Veryazov, V.; Widmark, P.-O.; Cossi, M.; Schimmelpfennig, B.; Neogrady, P.; Seijo, L. MOLCAS: a Program Package for Computational Chemistry. *Comput. Mater. Sci.* **2003**, *28*, 222−239.

(66) Zirak, P.; Penzkofer, A.; Mathes, T.; Hegemann, P. Photo-Dynamics of Roseoflavin and Riboflavin in Aqueous and Organic Solvents. *Chem. Phys.* **2009**, *358*, 111−122.

(67) Daidone, I.; Amadei, A.; Aschi, M.; Zanetti-Polzi, L. On the Nature of Solvatochromic Effect: The Riboflavin Absorption Spectrum as a Case Study. *Spectrochim. Acta Mol. Biomol. Spectrosc.* **2018**, *192*, 451−457.

(68) Metternich, J. B.; Mudd, R. J.; Gilmour, R. Flavins in Photocatalysis. In *Science of Synthesis*; De Vries, J. G., Ed.; Georg Thieme Verlag, 2018; Vol. *6*, pp 391−404.

(69) Bowd, A.; Byrom, P.; Hudson, J. B.; Turnbull, J. H. ExcitedD States of Flavine Coenzymes-III. Fluorescence and Phosphorescence Emissions. *Photochem. Photobiol.* **1968**, *8*, 1−10.

(70) Grodowski, M. S.; Veyret, B.; Weiss, K. Photochemistry of Flavins. Ii. Photophysical Properties of Alloxazines and Isoalloxazines. *Photochem. Photobiol.* **1977**, *26*, 341−352.

(71) Astanov, S.; Sharipov, M. Z.; Fayzullaev, A. R.; Kurtaliev, E. N.; Nizomov, N. Spectroscopic study of photo and thermal destruction of riboflavin. *J. Mol. Struct.* **2014**, *1071*, 133−138.

(72) Uoyama, H.; Goushi, K.; Shizu, K.; Nomura, H.; Adachi, C. Highly efficient organic light-emitting diodes from delayed fluorescence. *Nature* **2012**, *492*, 234−238.

(73) Aizawa, N.; Harabuchi, Y.; Maeda, S.; Pu, Y. J. Kinetic prediction of reverse intersystem crossing in organic donor-acceptor molecules. *Nat. Commun.* **2020**, *11*, 3909.

(74) Wang, Y. L.; Yeung, V.; Corradini, M. G.; Ludescher, R. D. Riboflavin as a Gras Luminescent Probe of Food and Pharmaceutical Quality. *Biophys. J.* **2016**, *110*, 490a−491a.

(75) Gai, F.; Hasson, K. C.; McDonald, J. C.; Anfinrud, P. A. Chemical Dynamics in Proteins: The Photoisomerization of Retinal in Bacteriorhodopsin. *Science* **1998**, *279*, 1886−1891.

(76) Gozem, S.; Schapiro, I.; Ferré, N.; Olivucci, M. The Molecular Mechanism of Thermal Noise in Rod Photoreceptors. *Science* **2012**, *337*, 1225−1228.

(77) Lee, H. H.; Senda, H.; Kuwae, A.; Hanai, K. Crystal and Molecular Structures of Allocinnamic Acid. *Bull. Chem. Soc. Jpn.* **1994**, *67*, 1475−1478.

(78) Lee, H. H.; Senda, H.; Oyama, K.; Kuwae, A.; Hanai, K. Crystal and Molecular Structures of a Low-Melting Polymorph of Allocinnamic Acid. *Bull. Chem. Soc. Jpn.* **1994**, *67*, 2574−2576.

(79) Hocking, M. B. Photochemical and Thermal Isomerizations of *cis*- and *trans*-Cinnamic Acids, and Their Photostationary State. *Can. J. Chem.* **1969**, *47*, 4567−4576.

(80) Turner, B.; Mueller-Harvey, I.; McAllan, B. A. Light-induced isomerization and dimerization of cinnamic acid derivatives in cell walls. *Phytochemistry* **1993**, *33*, 791−796.

(81) Wenger, O. S. Proton-Coupled Electron Transfer with Photoexcited Metal Complexes. *Acc. Chem. Res.* **2013**, *46*, 1517−1526.

(82) Cukier, R. I.; Nocera, D. G. Proton-Coupled Electron Transfer. *Annu. Rev. Phys. Chem.* **1998**, *49*, 337−369.

(83) Hammes-Schiffer, S.; Iordanova, N. Theoretical Studies of Proton-Coupled Electron Transfer Reactions. *Biochim. Biophys. Acta* **2004**, *1655*, 29−36.

(84) Hammes-Schiffer, S. Proton-Coupled Electron Transfer: Classification Scheme and Guide to Theoretical Methods. *Energy Environ. Sci.* **2012**, *5*, 7696−7703.

(85) Miller, D. C.; Tarantino, K. T.; Knowles, R. R. Proton-Coupled Electron Transfer in Organic Synthesis: Fundamentals, Applications, and Opportunities. *Top. Curr. Chem.* **2016**, *374*, 30.